https://doi.org/10.1016/j.rcim.2016.08.003

# Kinematics analysis of a hybrid manipulator for computer controlled ultra-precision freeform polishing

Peng Xu [a, b], Chi-Fai Cheung [a*], Bing Li [b*], Lai-Ting Ho[a], Ju-Fan Zhang [b]

[a] *Partner State Key Laboratory of Ultra-precision Machining Technology, Department of Industrial and Systems Engineering, The Hong Kong Polytechnic University, Hung Hom, Kowloon, Hong Kong*

[b] *School of Mechanical Engineering and Automation, Shenzhen Graduate School, Harbin Institute of Technology, Shenzhen 518055, China*

## ABSTRACT

This paper presents a novel hybrid manipulator for computer controlled ultra-precision (CCUP) freeform polishing. The hybrid manipulator is composed of a three degree-of-freedom (DOF) parallel module, a two DOF serial module and a turntable providing a redundant DOF. The serial module holds the polishing tool and gives it no translations on the polishing contact area due to its particular mechanical design. The parallel module gives the workpiece three translations without rotations. A kinematics model is established for analyzing the kinematics of the parallel module and the serial module, respectively. For the parallel module, the inverse kinematics, forward kinematics, Jacobian matrix, workspace and dexterity distribution are analyzed systematically. Workspaces are generated for varying structural parameters. For the serial module, a kinematics model is established and the workspace is investigated. An example of saddle surface finishing with this manipulator is given and the movement of actuators with respect to this shape is analyzed theoretically. The results show that the proposed hybrid manipulator is a very suitable machine structure for CCUP freeform polishing.

*Keywords:* kinematics; hybrid manipulator; ultra-precision polishing, freeform surface, precession motion

---

* Corresponding authors.

E-mail addresses: benny.cheung@polyu.edu.hk (C.F. Cheung), libing.sgs@hit.edu.cn (B. Li)

## 1 Introduction

Freeform surfaces are widely used in many industries [1-4] for high precision optics, semiconductor applications, precision molds and orthopedic joints. However, no matter how precise the milling or grinding process is, it will inevitably leave cusps and stripes on the workpiece during the manufacturing of freeform surfaces. These marks or specific patterns must be removed by polishing process. Polishing is usually one of the final machining processes in precision machining to remove surface and subsurface damage from a ground part and correct its form [5].

Due to the geometrical complexity of freeform surfaces, polishing these surfaces is more challenging and difficult than polishing flat and spherical surfaces. Nowadays, many freeform surfaces are still polished manually, which means that the process not only relies heavily on the expertise and experience of the operator, but also requires much attention be given to processing and testing. To achieve a given level of precision with high efficiency and reliability, process automation is clearly the way forward.

In recent years, various approaches to automated polishing have been developed, including computer-controlled polishing (CCP) [3-6], stressed-lap polishing (SLP) [7, 8], plasma polishing [9, 10], and magnetorheological fluid polishing (MFP) [11, 12]. CCP is widely used and is regarded as an efficient polishing method. However, it has significant shortcomings for ultra-precision polishing of freeform surfaces. Due to the small size of the polishing tool, high-frequency errors may be produced. If the size of the polishing tool is increased, the polishing tool and the surface may not fit well, which results in poor quality finishing. SLP technology can overcome this problem. The tool can be actively deformed by on-board actuators to conform to the target surface. However, this results in a very complex tooling, control system and a weak capability to correct errors of form. Plasma polishing is a non-contact polishing method that can overcome the shortcomings of traditional contact polishing methods, but it has low polishing efficiencies and high environmental requirements for processing. MFP is a flexible polishing technology that can achieve high precision, but its cost is high and it is difficult to polish concave surface and high steepness surfaces using this technology.

CCUP based on precession polishing is a novel polishing method proposed and developed by Walker et al. [13, 14]. Unlike traditional CCP technology, the precession polishing process makes use of compliant tooling controlled by air pressure. Due to the compliance of the tool, the fit problem between the tooling and the workpiece in the traditional CCP polishing method can be solved. The position and orientation of tooling in space is orchestrated by a machine tool with an open kinematic chain and serially connected links. Zeeko Ltd. has developed a series of Intelligent Robotic Polishers (IRP) for this process. However, the constructions of these machines are based on serial manipulators. The motions of the actuators require high accuracy because of the cumulative error effect of the serial manipulator. Furthermore, to minimize processing time, the machine needs to achieve maximum linear traverse speed, which imposes stringent requirements on the machine dynamics.

A parallel manipulator is one in which there exist two or more closed kinematic chains linking the base to the end effector. The parallel manipulator has some favorable characteristics compared to the serial manipulator, such as higher stiffness, high dynamic performance, superior accuracy, low mobile masses and greater load-to-weight ratio, allowing a wide range of applications as an industrial robot and machine tool [15-20]. The most notable shortcoming of parallel manipulators is their relatively small workspaces compared with their serial counterparts. However, in an ultra-precision polishing machine in which accuracy, stiffness and dynamic performance are more important than the size of the workspace, a parallel manipulator is an alternative to a serial manipulator.

A hybrid manipulator can be a combination of a parallel manipulator and a serial manipulator or a sequence of parallel manipulators [21-24]. A hybrid manipulator can provide the features and possess the advantages of both serial and parallel manipulators. In this study, a new polishing machining structure is proposed based on the precession polishing process. It is a hybrid manipulator combining a three DOF parallel module and a two DOF serial module. It is believed that a machine with the proposed hybrid structure can enhance accuracy and stiffness compared to a multi-axis serial structure.

Kinematics analysis is a common basis for mechanical design and control system development. Generally, CAM systems generate tool paths by indicating the tool tip coordinates and the tool axis orientation vectors in the workpiece coordinate system. These data are transformed into position commands for the linear and rotary actuators in the machine coordinate system by the kinematics model of the machine tool [25]. As a result, the kinematic model of the machine is the key to solving the trajectory control problem. The feed rate control, precision control, and geometric error compensation also have to use the kinematic model of the machine.

The remainder of the paper is organized as follows. The principle of the precession polishing process is introduced in Section 2, and the novel polishing machine with a hybrid manipulator is presented in Section 3. Section 4 addresses the kinematics problems of the parallel manipulator, and the kinematics problems of the serial manipulator are resolved in Section 5. Section 6 gives an example of the movement of the actuators in the proposed hybrid manipulator with respect to a saddle surface. Section 7 presents some conclusions.

## 2 Precession polishing process

During the polishing process, the polishing tool is rotated about its axis as shown in Fig.1. In the traditional polishing process, the polishing tool is vertical to the surface. As a result, the velocity profile has a zero point at the center of the contact area between the tool and the workpiece. According to the Preston law [26], the influence function is not mathematically well-behaved and is not optimized for form control algorithms.

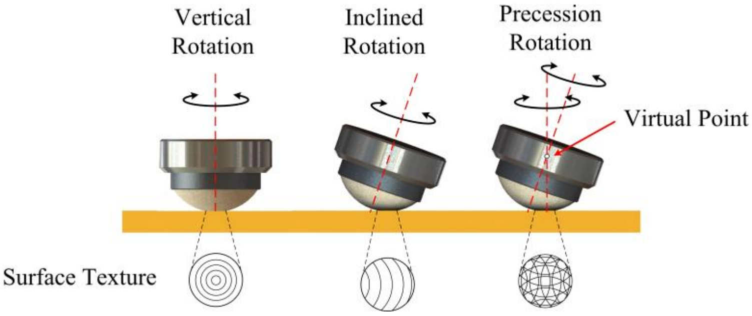

Fig. 1 Precession polishing process

In a precession polishing process [13, 14], the rotation-axis of the polishing tool is inclined to the surface's local normal direction. The precession polishing process makes use of a compliant spherical shaped polishing tool and polishes with the side of the tool. As a result, the point with zero velocity is shifted outside the contact area. To obtain a uniform surface texture with no directional properties, the tool axis is then precessed about the local normal direction of the surface. Precession averages the polishing texture, providing a tool influence function that is mathematically well-behaved and close to a Gaussian-like polishing influence function.

## 3 Hybrid manipulator for CCUP freeform polishing

### 3.1 Structure of the hybrid manipulator

To polish a freeform surface, the polishing machine should have five DOFs including three traditional DOF and two rotational DOF. The layout of the mechanical structure, transmission system and driving system all directly affect the performance of the machine. In this study, the proposed polishing machine consists of a parallel module and a serial module using a hybrid manipulator as shown in Fig. 2.

The moving platform of the parallel module is connected to the base by three identical serial chains. Each of the three chains contains one spatial parallelogram, and the vertices of which are four ball joints. The parallelogram is connected to the base by a prismatic joint. The output can be obtained through a combination of the actuation to the three prismatic joints. A fixture that holds the workpiece is mounted on the moving platform. It can be rotated to provide the rotation motion of the workpiece when polishing axially symmetric surfaces. To improve the stiffness and workspace performance of the parallel module, the three guideways are inclined and intersect at a vertex.

The serial manipulator consists of a rotating/tilting table and a polishing tool. The table is used to rotate the polishing tool about two orthogonal axes. The rotating axis is vertical and the tilting axis is horizontal to the base. The curvature center of the tool head coincides with the virtual pivot intersected by the two axes.

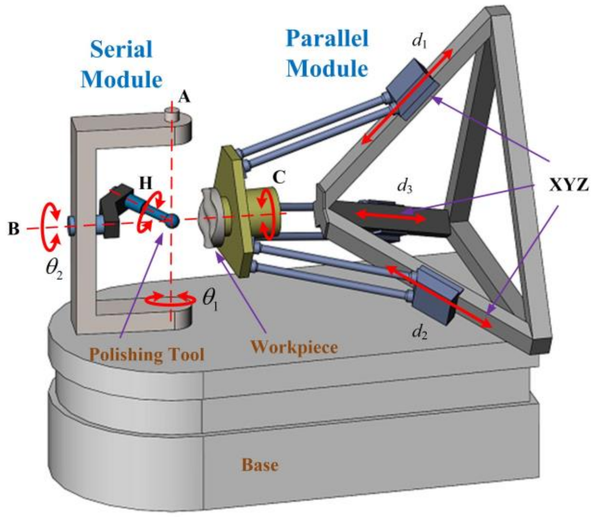

Fig. 2 Configuration of the proposed machine with hybrid manipulator for CCUP freeform polishing

### 3.2 Mobility

The first issue to address in the design of the manipulator is its motion capability. The output motion of the serial module is obvious when the input joints are actuated. The output motion of the parallel module should be designed to have three translational DOF with respect to the base. There are twelve ball joints, three prismatic joints and eleven links, including the base. Applying the Grübler-Kutzbach formula [27]

$$M = 6(n - g - 1) + \sum_{i=1}^{n} f_i \ , \tag{1}$$

where $n$ is the number of links, $g$ is the number of joints, and $f_i$ represents the DOF of joint $i$ ($1<i<g$), yields a mobility of nine. Due to the arrangement of the links and joints, each leg's motion is restricted only by ball joints at both ends as shown in Fig. 2. Each leg is thus free to rotate around its axis and six idle DOF exist within the parallel module. Hence, it leaves the parallel module with three DOF.

### 3.3 Applications and novelties

The machine tool provides the following motions. (1) X, Y, Z: positioning the workpiece in the required location; (2) A, B: orientation of the polishing head to follow the local normal direction of the surface and impose the precession angle; (3) H-axis: rotation of the polishing head to create the tool influence function; (4) C-axis: rotation of the fixture to impose rotational symmetry if required (a redundant DOF). This design provides the capability to polish circular and non-circular surfaces, flat, aspherical, off-axis aspherical and freeform surfaces and any tool paths can be implemented.

As the three rotation axes of the serial module intersect at a virtual pivot, rotations in A and B preserve the same polishing contact area between the polishing tool and the workpiece, causing no translations along X, Y and Z direction. As a result, the motions are decoupled. The positions are all controlled by the parallel module and the orientations are all determined by the serial module. This feature benefits motion control system development.

Freeform surface workpieces are stringent in terms of machine dynamic performance, as maximum linear traverse speed is required to minimize the polishing time. Unlike the traditional serial X-Y-Z Cartesian mechanism, the three actuators of the parallel module are placed on a fixed base and do not move during the polishing process. This enables the moving platform to bear a relatively small load and inertia, so the machine can obtain high dynamic performance to increase the acceleration and velocity limitations of the end effector and thus improve polishing efficiency. Moreover, having actuators on the base also contributes to obtaining good thermal behavior.

## 4 Kinematics analysis of the parallel module

### 4.1 Inverse kinematics

The inverse kinematics problem involves mapping a known pose of the output platform of the manipulator to a set of input joint variables that achieve the pose. A schematic diagram of the parallel module is shown in Fig. 3. The center of the ball joint that connects the legs to the slider in each of the three chains is denoted as $C_i$, and the center of the ball joint connected to the legs with the moving platform in each chain is denoted as $D_i$. A fixed global reference frame denoted as $O$-$XYZ$ is located at the center of the regular $\triangle A_1A_2A_3$ with the $Z$-axis normal to the base and the $X$-axis directed along $OA_1$. Another reference frame, denoted as $P$-$uvw$, is located at the center of the regular $\triangle D_1D_2D_3$. The $w$-axis is perpendicular to the output platform and the $u$-axis is directed along $PD_1$. Related geometric parameters are $OA_i = a$, $PD_i = b$, $B_iC_i = c$ and $C_iD_i = L$, where $i = 1$, 2, 3. The angle between $OA_i$ and the linear guideways $A_iN$ is $\alpha$.

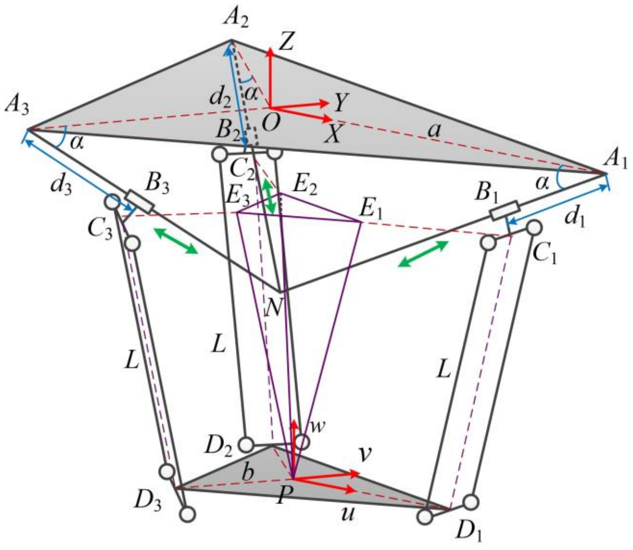

Fig. 3 Schematic diagram of the parallel module

The objective of inverse kinematics is to define a mapping from the pose of reference point $P$ in a Cartesian space to the set of actuated inputs $d_i$ that achieves that pose. The position vector of point $P$ in frame $O$-$XYZ$ can be expressed as

$$\boldsymbol{P} = \begin{bmatrix} x & y & z \end{bmatrix}^{\mathrm{T}}. \tag{2}$$

As shown in Fig. 3, the coordinate of the point $A_i$, $B_i$, $C_i$ in the frame $O$-$XYZ$ can be described by the vector $\boldsymbol{A}_i$, $\boldsymbol{B}_i$, $\boldsymbol{C}_i$, which can be written as

$$\boldsymbol{A}_i = \begin{bmatrix} a\cos\eta_i \\ a\sin\eta_i \\ 0 \end{bmatrix}, \quad \boldsymbol{B}_i = \begin{bmatrix} (a - d_i\cos\alpha)\cos\eta_i \\ (a - d_i\cos\alpha)\sin\eta_i \\ -d_i\sin\alpha \end{bmatrix}, \quad \boldsymbol{C}_i = \begin{bmatrix} (a - d_i\cos\alpha + c\sin\alpha)\cos\eta_i \\ (a - d_i\cos\alpha + c\sin\alpha)\sin\eta_i \\ -d_i\sin\alpha - c\cos\alpha \end{bmatrix}, \tag{3}$$

and the coordinate of the point $D_i$ in the frame *P-uvw* can be described by the vector ${}^{P}\boldsymbol{D}_i$, which can be expressed as

$${}^{P}\boldsymbol{D}_i = \begin{bmatrix} b\cos\eta_i & b\sin\eta_i & 0 \end{bmatrix}^{\mathrm{T}}, \tag{4}$$

where

$$\eta_i = \frac{2(i-1)}{3}\pi \tag{5}$$

is the angle between the line $OA_i$ and *X*-axis or $PD_i$ and *u*-axis.

As there are no rotations of the moving platform, vectors ${}^{P}\boldsymbol{D}_i$ in frame *O-XYZ* can be written as

$$\boldsymbol{D}_i = \boldsymbol{T}\,{}^{P}\boldsymbol{D}_i + \boldsymbol{P} = \begin{bmatrix} b\cos\eta_i + x & b\sin\eta_i + y & z \end{bmatrix}^{T}, \tag{6}$$

where $\boldsymbol{T}$ stands for a unit matrix of order 3.

Then the inverse kinematics of the parallel module can be solved by writing the following constraint equation

$$\left|\boldsymbol{D}_i - \boldsymbol{C}_i\right| = L. \tag{7}$$

That is

$$(x - x_i)^2 + (y - y_i)^2 + (z - z_i)^2 = L^2, \tag{8}$$

where

$$x_i = -d_i\cos\alpha\cos\eta_i + R\cos\eta_i, \quad y_i = -d_i\cos\alpha\sin\eta_i + R\sin\eta_i, \quad z_i = -d_i\sin\alpha - c\cos\alpha,$$

$$R = a - b + c\sin\alpha. \tag{9}$$

The inputs of the parallel module $d_i$ can be solved from Eq. (8) when the geometric parameters are given. It should be noted that there are two solutions for each chain. Hence, there are totally eight inverse kinematics solutions for a given position of the parallel module. In this study, only the configuration shown in Fig. 3 is considered.

### 4.2 Forward kinematics

The forward kinematics problem involves mapping from a known set of input joint variables to a pose of the moving platform that results from those given inputs. From Eq. (8), if the input parameter $d_i$ is specified, one can see that the equations represent three spheres with the center at $C_i$ and radii $L$. The position of point $P$ can be obtained by finding the intersection point of three spherical surfaces [28, 29]. Another straightforward kinematic model is proposed in this paper. It adopts the spatial geometry and vector algebra method to solve the forward kinematic problems. Compared with the equations-based method, the derivation process of the proposed method is concise and direct.

As shown in Fig. 3, $C_i$ is removed to $E_i$ along vector $\boldsymbol{D_iP}$. Then, $E_i$ and $P$ compose a tetrahedron as shown in Fig. 4. From a mathematical point of view, the forward kinematics problem of the parallel module is reduced to calculate the fourth point of a tetrahedron when the other three points and the edge lengths are known.

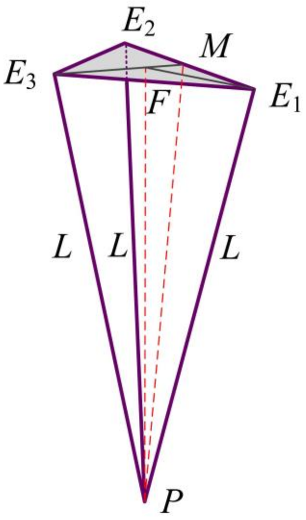

Fig. 4 Schematic of the forward kinematics

Let $F$ be the projection of vertex $P$ on the plane, which is constituted by $E_i$ expressed as

$$\boldsymbol{E}_i = \begin{bmatrix} \left(a - d_i \cos\alpha + c\sin\alpha - b\right)\cos\eta_i \\ \left(a - d_i \cos\alpha + c\sin\alpha - b\right)\sin\eta_i \\ -d_i \sin\alpha - c\cos\alpha \end{bmatrix}, \tag{10}$$

and $M$ be the center of line $E_1E_2$, which can be expressed as

$$\boldsymbol{M} = \frac{\boldsymbol{E}_1 + \boldsymbol{E}_2}{2}. \tag{11}$$

As $\triangle PE_1E_2$ is an isosceles triangle, $PM$ is perpendicular to $E_1E_2$. Based on the theorem of three perpendiculars, $FM$ is perpendicular to $E_1E_2$. Similar results can be derived on the other two edges. As a result, $F$ is the circumcenter of $\triangle E_1E_2E_3$ and the position vector of $F$ can be obtained as

$$\boldsymbol{F} = \boldsymbol{M} + \boldsymbol{MF}. \tag{12}$$

The vector $\boldsymbol{MF}$ can be expressed as

$$\boldsymbol{MF} = \left|\boldsymbol{MF}\right| \boldsymbol{n}_{MF}, \tag{13}$$

where $|\boldsymbol{MF}|$ is the norm and $\boldsymbol{n}_{MF}$ is the unit vector.

$|\boldsymbol{MF}|$ can be derived as

$$\left|\boldsymbol{MF}\right| = \sqrt{\left|\boldsymbol{E}_1\boldsymbol{F}\right|^2 - \left|\boldsymbol{E}_1\boldsymbol{M}^2\right|}, \tag{14}$$

where

$$\left|\boldsymbol{E}_1\boldsymbol{F}\right| = \frac{\left|\boldsymbol{E}_1\boldsymbol{E}_2\right|\left|\boldsymbol{E}_2\boldsymbol{E}_3\right|\left|\boldsymbol{E}_3\boldsymbol{E}_1\right|}{4S} \tag{15}$$

represents the circumcircle radius of $\triangle E_1E_2E_3$, in which

$$S = \sqrt{q(q - \left|\boldsymbol{E}_1\boldsymbol{E}_2\right|)(q - \left|\boldsymbol{E}_2\boldsymbol{E}_3\right|)(q - \left|\boldsymbol{E}_3\boldsymbol{E}_1\right|)}, \quad q = \frac{1}{2}\left(\left|\boldsymbol{E}_1\boldsymbol{E}_2\right| + \left|\boldsymbol{E}_2\boldsymbol{E}_3\right| + \left|\boldsymbol{E}_3\boldsymbol{E}_1\right|\right). \tag{16}$$

$\boldsymbol{n}_{MF}$ can be derived as

$$\boldsymbol{n}_{MF} = \frac{\boldsymbol{E}_1\boldsymbol{E}_2 \times \boldsymbol{E}_2\boldsymbol{E}_3 \times \boldsymbol{E}_1\boldsymbol{E}_2}{\left|\boldsymbol{E}_1\boldsymbol{E}_2\right| \times \left|\boldsymbol{E}_2\boldsymbol{E}_3\right| \times \left|\boldsymbol{E}_1\boldsymbol{E}_2\right|}. \tag{17}$$

When the position of $F$ is obtained, the point $P$ can be derived as

$$\boldsymbol{P} = \boldsymbol{F} + \boldsymbol{FP}. \tag{18}$$

The vector $\boldsymbol{FP}$ can be expressed as

$$\boldsymbol{FP} = |\boldsymbol{FP}|\boldsymbol{n}_{FP}, \tag{19}$$

where $|\boldsymbol{FP}|$ is the norm and $\boldsymbol{n}_{FP}$ is the unit vector.

$|\boldsymbol{FP}|$ and $\boldsymbol{n}_{FP}$ can be derived as

$$|\boldsymbol{FP}| = \sqrt{L^2 - |\boldsymbol{E}_1\boldsymbol{F}|^2}, \quad \boldsymbol{n}_{FP} = \frac{\boldsymbol{E}_1\boldsymbol{E}_2 \times \boldsymbol{E}_2\boldsymbol{E}_3}{|\boldsymbol{E}_1\boldsymbol{E}_2||\boldsymbol{E}_2\boldsymbol{E}_3|}. \tag{20}$$

At this point, the forward kinematic model of the parallel module is established.

### 4.3 Jacobian matrix analysis

The Jacobian matrix is defined as the matrix that maps the relationship between the output velocity of the moving platform and the input velocities of the actuated joints. Eq. (8) can be differentiated with respect to time to obtain the velocity equations, which leads to

$$\boldsymbol{J}^{inv}\dot{\boldsymbol{d}} = \boldsymbol{J}^{dir}\dot{\boldsymbol{X}}, \tag{21}$$

where $\dot{\boldsymbol{X}}$ and $\dot{\boldsymbol{d}}$ are respectively the vector of output velocities and the vector of input velocities defined as

$$\dot{\boldsymbol{X}} = \begin{bmatrix}\dot{x} & \dot{y} & \dot{z}\end{bmatrix}^{\mathrm{T}}, \quad \dot{\boldsymbol{d}} = \begin{bmatrix}\dot{d}_1 & \dot{d}_2 & \dot{d}_3\end{bmatrix}^{\mathrm{T}}, \tag{22}$$

$\boldsymbol{J}^{inv}$ is the inverse Jacobian matrix expressed as

$$\boldsymbol{J}^{inv} = \mathrm{diag}\left(d_{11}, d_{22}, d_{33}\right), \tag{23}$$

where

$$\begin{gathered} d_{11} = x\cos\alpha + z\sin\alpha - a\cos\alpha + b\cos\alpha + d_1, \\ d_{22} = -\frac{1}{2}x\cos\alpha + \frac{\sqrt{3}}{2}y\cos\alpha + z\sin\alpha - a\cos\alpha + b\cos\alpha + d_2, \\ d_{33} = -\frac{1}{2}x\cos\alpha - \frac{\sqrt{3}}{2}y\cos\alpha + z\sin\alpha - a\cos\alpha + b\cos\alpha + d_3, \end{gathered} \tag{24}$$

and $\boldsymbol{J}^{dir}$ is the direct Jacobian matrix expressed as

$$\boldsymbol{J}^{dir} = \begin{bmatrix} x_1 & y_1 & z_1 \\ x_2 & y_2 & z_2 \\ x_3 & y_3 & z_3 \end{bmatrix}, \tag{25}$$

where

$$x_1 = -a + d_1\cos\alpha - c\sin\alpha + x + b\,,\quad y_1 = y\,,\quad z_1 = d_1\sin\alpha + c\cos\alpha + z\,,$$

$$x_2 = \frac{1}{2}a - \frac{1}{2}d_2\cos\alpha + \frac{1}{2}c\sin\alpha + x - \frac{1}{2}b\,,\quad y_2 = -\frac{\sqrt{3}}{2}a + \frac{\sqrt{3}}{2}d_2\cos\alpha - \frac{\sqrt{3}}{2}c\sin\alpha + y + \frac{\sqrt{3}}{2}b\,,$$

$$z_2 = d_2\sin\alpha + c\cos\alpha + z\,,$$

$$x_3 = \frac{1}{2}a - \frac{1}{2}d_3\cos\alpha + \frac{1}{2}c\sin\alpha + x - \frac{1}{2}b\,,\quad y_3 = \frac{\sqrt{3}}{2}a - \frac{\sqrt{3}}{2}d_3\cos\alpha + \frac{\sqrt{3}}{2}c\sin\alpha + y - \frac{\sqrt{3}}{2}b\,,$$

$$z_3 = d_3\sin\alpha + c\cos\alpha + z\,. \tag{26}$$

When the manipulator is away from singularities, the following velocity equation can be derived from Eq. (21)

$$\dot{\boldsymbol{d}} = \boldsymbol{J}\dot{\boldsymbol{X}} \tag{27}$$

where

$$\boldsymbol{J} = \boldsymbol{J}^{-inv}\boldsymbol{J}^{div} = \begin{bmatrix} \frac{x_1}{d_{11}} & \frac{y_1}{d_{11}} & \frac{z_1}{d_{11}} \\ \frac{x_2}{d_{22}} & \frac{y_2}{d_{22}} & \frac{z_2}{d_{22}} \\ \frac{x_3}{d_{33}} & \frac{y_3}{d_{33}} & \frac{z_3}{d_{33}} \end{bmatrix}_{3\times 3}. \tag{28}$$

is defined as the Jacobian matrix of the parallel module.

### 4.4 Workspace analysis

As mentioned, parallel manipulators have relatively small workspaces. As a result, the workspace of a parallel module is one of the most important factors reflecting machine working capacity, and it is necessary to analyze the shape and volume of the workspace to determine the size of workpiece that can be polished. Moreover, it is essential to investigate the relationship between the workspace and the structural parameters to guide the mechanical design. The workspace is defined as the space that can be achieved by the three translations of point *P* in the global reference frame *O-XYZ*. The geometric method [30] and the numerical method [15] are used to obtain the workspace in this paper.

From Eq. (8), it can be seen that the workspace of each chain is a set of spheres with radii $L$ when the actuators move. As a result, the workspace of each chain is an enveloping solid of these spheres whose centers move along the line between $d_{min}$ and $d_{max}$. As the parallel module has three chains, the workspace can be derived geometrically by the intersection of three such enveloping solids as shown in Fig. 5.

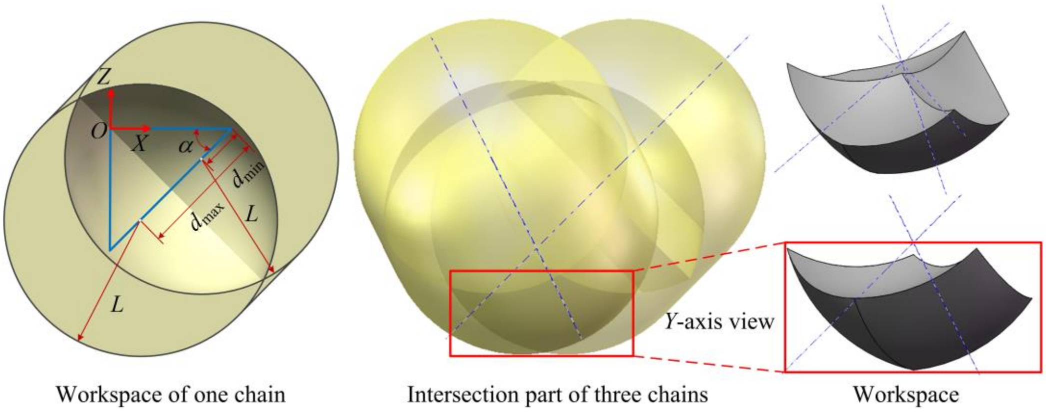

Workspace of one chain

Intersection part of three chains

Workspace

Fig. 5 Workspace of the parallel module obtained from geometric method

To facilitate the analysis of dexterity, a numerical approach using a search method in an anticipated area is also adopted to obtain the workspace. From Fig. 5, it can be seen that voids exist within the workspace. This requires special attention when the search method and workspace volume calculation are used in cylindrical coordinates. The related structural parameters of the parallel module are listed in Table 1. The flowchart to determine the workspace is shown in Fig. 6. A cylinder with a height range from -800 mm to -300 mm and a radius of 400 mm is selected as the search area. The cylinder is divided into a number of layers along the $Z$-axis with a resolution of $\Delta Z$ = 5 mm. A number of grid points are then generated in each layer with a resolution of $\Delta R$ = 5 mm and $\Delta \theta$ = 3°. The active prismatic joint positon $d_i$ for each grid point is calculated by using the inverse kinematics model and checked to see if it is within the motion range. The three-dimensional shape of all boundary points constituting the workspace is shown in Fig. 7.

Table 1 Parameters of the parallel module

| Parameters | Value | Parameter | Value |
|---|---|---|---|
| $a$ | 400 mm | $\alpha$ | 45° |
| $b$ | 100 mm | $d_{min}$ | 141.4 mm |
| $c$ | 0 mm | $d_{max}$ | 424.3 mm |
| $L$ | 447.2 mm | | |

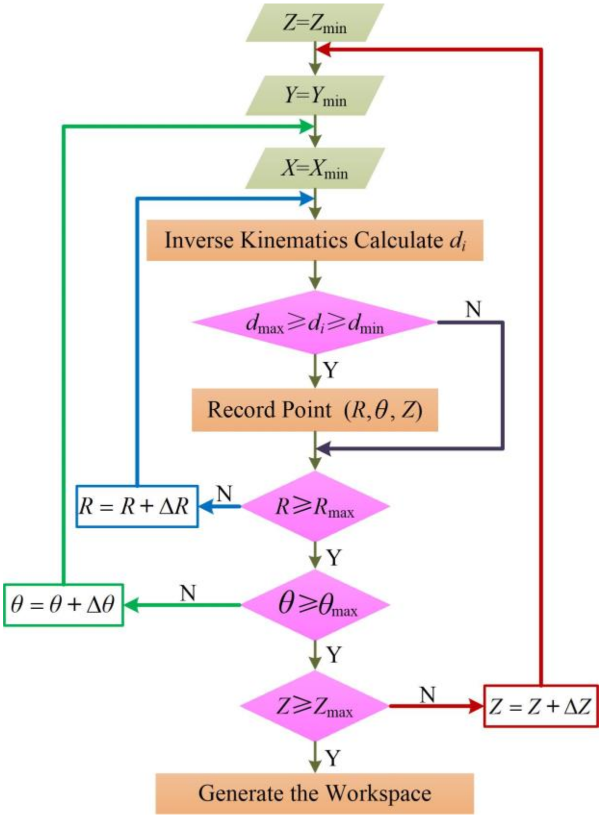

Fig. 6 Flowchart to determine the workspace

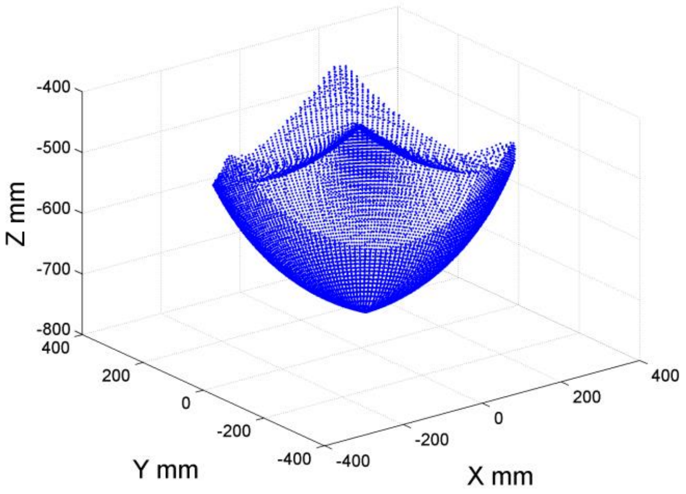

Fig. 7 Workspace of the parallel module obtained from numerical method

From both the geometric method and the numerical method, it can be seen that the shape of the workspace is 120° symmetric about the $Z$-axis. This is consistent with the global reference frame and the symmetrical structure of the parallel module. The coordinates of the extreme values of the reachable workspace are: $X \in$ [-314 mm, 310 mm], $Y \in$ [-298 mm, 298 mm], and $Z \in$ [-735 mm, -432 mm]. The total workspace volume is approximately calculated as the sum of the subworkspace and the subworkspace volume on each layer $V_i$, which can be expressed as

$$V_i = \frac{1}{2}\sum_{j}^{n} \rho_j^2 \Delta\gamma \Delta Z \ , \tag{29}$$

where $\rho_j$ is the polar radius of the boundary, $\Delta\gamma$ is the polar angle increment and $\Delta Z$ is the height increment.

There are five main structural parameters ($a$, $b$, $c$, $L$, $\alpha$) for the parallel module. It is necessary to identify the effect of varying the structural parameters on the workspace. The workspace volumes of the parallel module with variation of structure parameter $b$ are shown in Fig. 8(a), which illustrates that the maximum workspace size occurs when $b$ is about 100 mm. Fig. 8(b) describes the variation in the tendency of workspace size with increasing actuator layout angle $\alpha$. It is observed that the maximum workspace volume occurs when $\alpha$ is around 45°.

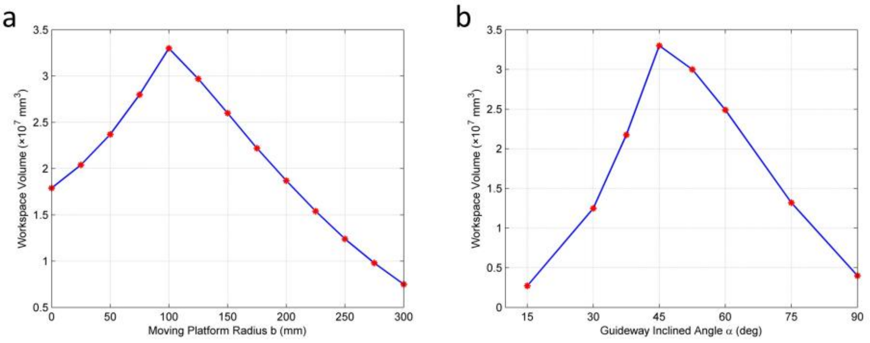

Fig. 8 Workspace volume varies with structural parameters. (a) Moving platform radius $b$. (b) Guideway inclined angle $\alpha$.

### 4.5 Dexterity analysis

The dexterity as well as isotropy of a parallel manipulator is frequently evaluated by the condition index, which is defined as the reciprocal of the condition number of the Jacobian matrix [31]. That is

$$\kappa(\boldsymbol{J}) = \|\boldsymbol{J}\| \|\boldsymbol{J}^{-1}\|, \ \eta(\boldsymbol{J}) = \frac{1}{\kappa(\boldsymbol{J})}, \tag{30}$$

where $\eta$ is the condition number of the Jacobian matrix, and $\|\cdot\|$ denotes the Euclidian norm of a matrix.

Condition number $\eta$ is an important issue for machine design, trajectory planning and control. $\eta$ is a value between 0 and 1. When $\eta = 0$, the manipulator is in its singular configuration, and $\eta = 1$ indicates its isotropic configuration. As $\eta$ is configuration dependent, with parameters as described in Table 1, the dexterity distributions in different planes in the workspace are shown in Fig. 9. From the figure, one can see that the workspaces at different cross-sections have different shapes and sizes. The dexterity distribution exhibits mirror symmetry with respect to the $X$-axis and 120° centrosymmetry with respect to the $Z$-axis. This is consistent with the global coordinate system and the structural characteristics of the parallel module. Moreover, dexterity is maximal when the moving platform lies along the $Z$-axis, and decreases when it approaches the boundary of the workspace in a plane at a given height.

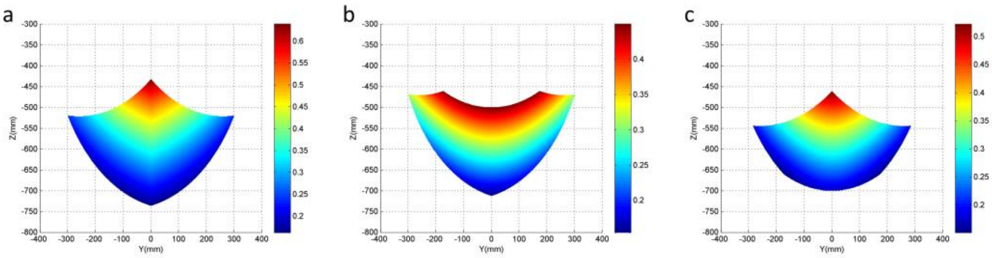

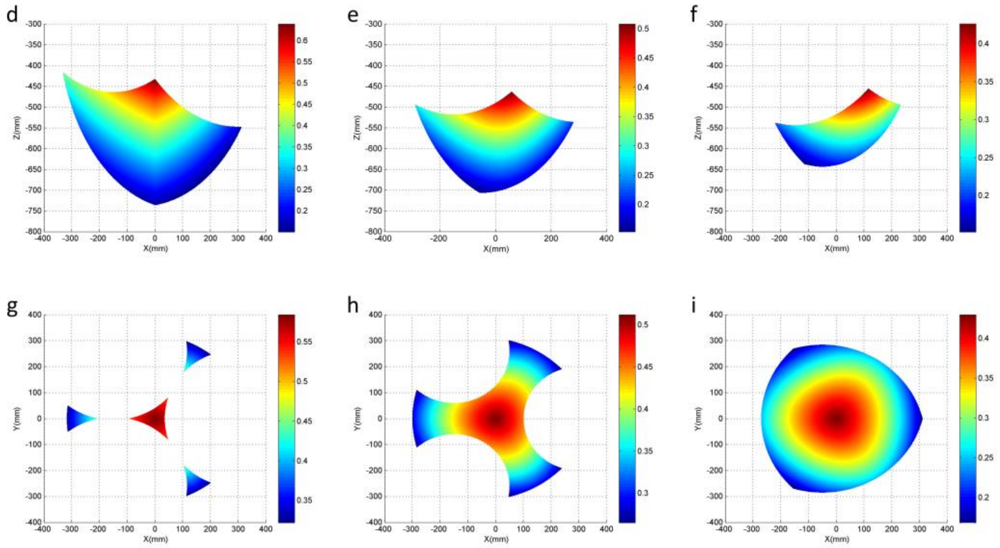

Fig. 9 Dexterity distribution in the workspace. (a) *O*-*YZ* plane with $x = 0$ mm. (b) *O*-*YZ* plane with $x = 100$ mm. (c) *O*-*YZ* plane with $x = -100$ mm. (d) *O*-*XZ* plane with $y = 0$ mm. (e) *O*-*XZ* plane with $y = 100$ mm. (f) *O*-*XZ* plane with $y = 200$ mm. (g) *O*-*XY* plane with $z = -460$ mm. (h) *O*-*XY* plane with $z = -500$ mm. (i) *O*-*XY* plane with $z = -550$ mm.

## 5 Kinematics analysis of the serial module

### 5.1 Forward and inverse kinematics

The schematic diagram of the serial module is shown in Fig. 10. As the rotations of *A* and *B* cause no translations of the tool head, a fixed global reference frame *o*-*xyz* is located at the center of the tool head with the *z*-axis along *A* and the *x*-axis along the initial direction of *B*. The rotation angles of *A* and *B* are, respectively, set as $\theta_1$ and $\theta_2$. The initial configuration is shown in Fig. 2. $\delta$ and $r$ are the structural parameters, which represent the angle between the axis of the polishing tool and the *x*-axis and the radius of the tool head, respectively. The rotational axis of the polishing tool intersects with the tool head at point *p*. The kinematics problem of the serial module is to find the corresponding orientation of the polishing tool when analyzing a random point being polished [32].

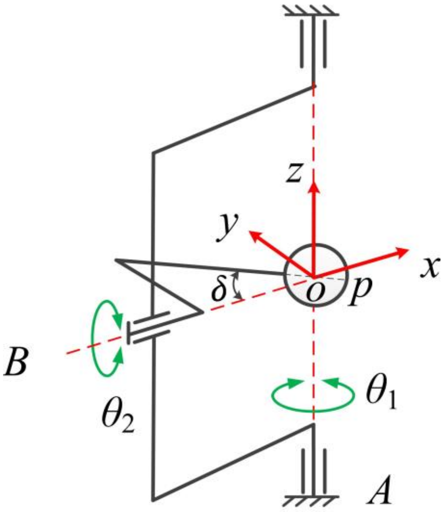

Fig. 10 Schematic diagram of the serial module

The forward kinematics problem is to map given angles $\theta_1$ and $\theta_2$ to the orientation of *op*. In the frame *o*-*xyz*, *p* can only rotate around the *x*-axis and the *z*-axis. The detailed kinematics schematic of the serial module can be solved by focusing on the polishing head. As shown in Fig. 11, *p* reaches $p_b$ after rotating $\theta_2$ around the *x*-axis and then reaches $p_a$ after rotating $\theta_1$ around the *z*-axis. The position vector of *p* and $p_a$ in the frame *o*-*xyz* can be written as

$$\boldsymbol{p} = [r\cos\delta \quad -r\sin\delta \quad 0]^{\mathrm{T}}, \quad \boldsymbol{p}_a = [x \quad y \quad z]^{\mathrm{T}}, \tag{31}$$

with the coordinate of $p_a$ under the following constraint

$$x^2 + y^2 + z^2 = r^2 . \tag{32}$$

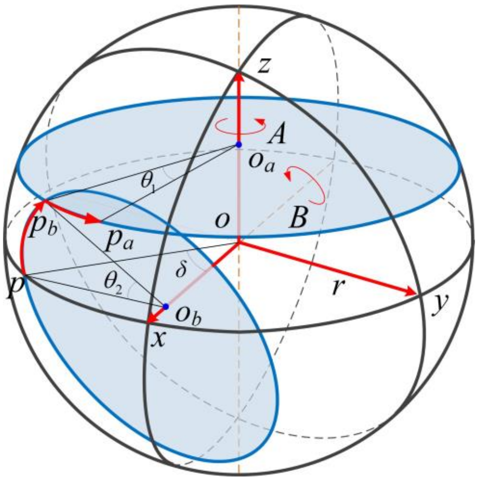

Fig. 11 Schematic of the forward kinematics

***p*** and ***p****$_a$* have the relation

$$\boldsymbol{p}_a = \boldsymbol{R}_{\theta_1\theta_2}\boldsymbol{p}\ , \tag{33}$$

where

$$\boldsymbol{R}_{\theta_1\theta_2} = \begin{bmatrix} \cos\theta_1 & -\sin\theta_1\cos\theta_2 & \sin\theta_1\sin\theta_2 \\ \sin\theta_1 & \cos\theta_1\cos\theta_2 & -\cos\theta_1\sin\theta_2 \\ 0 & \sin\theta_2 & \cos\theta_2 \end{bmatrix} \tag{34}$$

is the rotation matrix due to the rotational angle $\theta_1$ and $\theta_2$.

The inverse kinematics problem aims to map a given orientation of *op* to the input angles $\theta_1$ and $\theta_2$. As shown in Fig. 12, *c* and *d* are the projected points of $p_a$ and $p_b$ on the *o*-*xy* plane. $o_1$ and *e* are the projected points of *c* and *d* the on the *x*-axis. $\theta_1$ and $\theta_2$ can be derived according to the geometric relationships

$$\theta_2 = -\arcsin\frac{P_b c}{P_b o_1} = -\arcsin\frac{P_a d}{po\sin\delta} = -\arcsin\frac{z}{r\sin\delta}\ , \tag{35}$$

$$\theta_1 = \psi - \xi = \arctan\frac{P_b c\cot\theta_2}{op\cos\delta} - \arctan\frac{de}{oe} = \arctan\left|\frac{z\cot\theta_2}{r\cos\delta}\right| - \arctan\left|\frac{y}{x}\right|, \tag{36}$$

in which the signs of $\theta_1$ and $\theta_2$ should be determined according to the quadrant of the coordinate system.

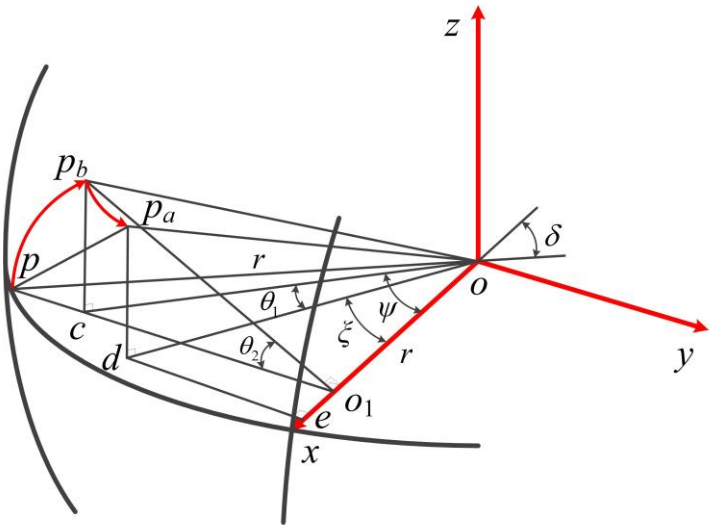

Fig. 12 Schematic of the inverse kinematics

### 5.2 Workspace analysis

To design the hybrid manipulator for the polishing machine, it is essential to analyze the workspace of the serial module, as it is similar to the parallel module. The workspace is defined as the space that can be reached by point *p*. The workspaces of the serial module with different input motion ranges when $\delta$=45° and *r*=20 mm are shown in Fig. 13.

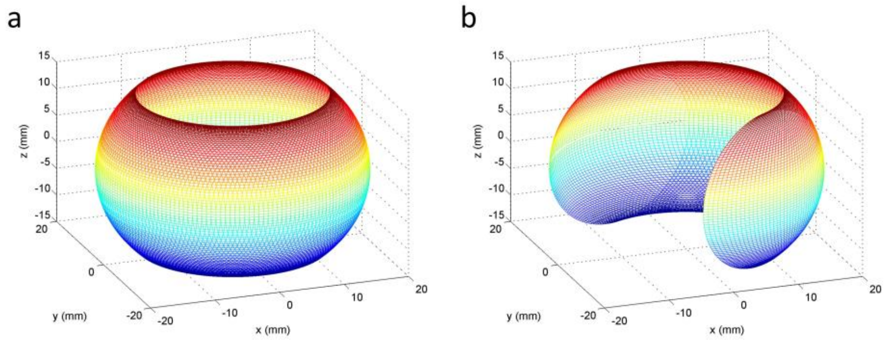

Fig. 13 Workspace of the serial module. (a) $\theta_1 \in$[-180°, 180°], $\theta_2 \in$[-180°, 180°]. (b) $\theta_1 \in$[-60°, 115°], $\theta_2 \in$[-180°, 180°]

The effect of structural parameters on the workspace should also be investigated. The top views of the workspace when $\theta_1 \in$[-60°, 115°] and $\theta_2 \in$[-180°, 180°] with the different $\delta$ are shown in Fig. 14, which illustrates that the workspace increases as $\delta$ is increased. When $\delta$ = 90°, *op* and the *y*-axis coincide and the workspace expands to fill the whole spherical surface.

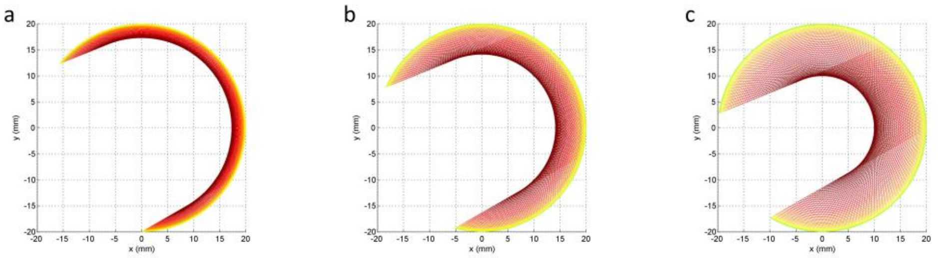

Fig. 14 Top view of the workspace with different $\delta$. (a) $\delta$=30°. (b) $\delta$=45°. (c) $\delta$=60°

### 5.3 Precession analysis

As shown in Fig. 15, the axis of the polishing tool should be inclined and rotate around the local normal direction of the surface with the precession angle $\rho$ during the polishing of freeform surfaces. The axis of the polishing tool changes constantly, but the polishing tool always maintains contact with the surface at a determined position because the tool's shape is spherical and the center remains unchanged. The precession trajectory can be regarded as the polishing tool's rotation around an arbitrary axis in space that is consistent with the local normal direction. The trajectory of the axis is a conical surface and the trajectory of $p$ is a circle.

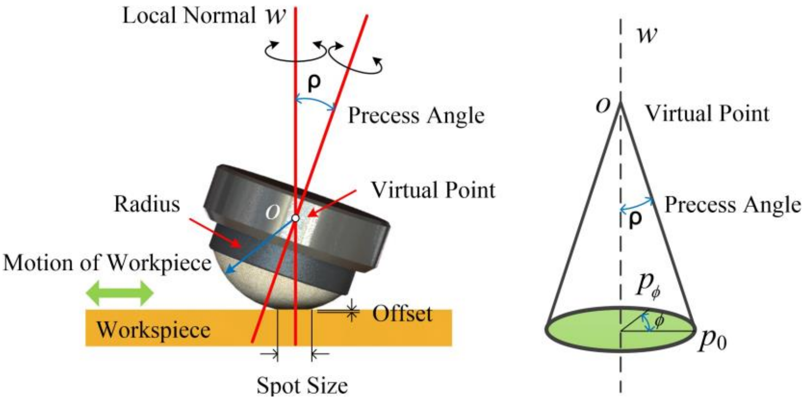

Fig. 15 Precession motion of the polishing tool

The motion schematic of the polishing tool axis is shown in Fig. 16. $\boldsymbol{p}_0$ ($x_0$, $y_0$, $z_0$) represents the initial position of $p$ during the precession process; $w$ is the arbitrary axis in space; $\alpha$ is the angle between the projection $on$ and the $x$-axis; $\beta$ is the angle between the $w$ and $z$-axis.

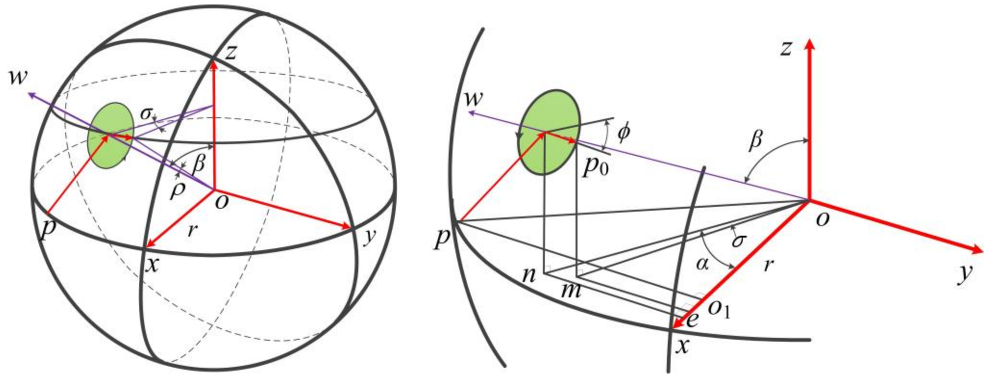

Fig. 16 Motion schematic of the polishing tool axis

The local normal unit vector of the polishing point is denoted as ($\lambda$, $\mu$, $\upsilon$). The relationship between angles $\alpha$ and $\beta$ of arbitrary axis $w$ in space and the unit vector ($\lambda$, $\mu$, $\upsilon$) can be expressed as

$$\alpha = \arctan\left|\frac{\mu}{\lambda}\right|, \quad \beta = \arccos \nu \tag{37}$$

in which the sign of the $\alpha$ should be determined according to the quadrant of the coordinate system.

$\boldsymbol{p}_0$ can be obtained by rotating $\boldsymbol{p}$ to coincide with the $w$-axis, and then rotating $\sigma$ around the $z$-axis. That is

$$x_0 = r\sin\beta\cos(\alpha-\sigma), \quad y_0 = r\sin\beta\sin(\alpha-\sigma), \quad z_0 = r\cos\beta, \tag{38}$$

where $\sigma$ is the projection of precession angle $\rho$ on the $o$-$xy$ plane and it can be expressed as

$$\sigma = \arcsin\frac{\sin\rho}{\sin\beta}. \tag{39}$$

With precession angle $\rho$, when the polishing tool axis rotates from $\boldsymbol{p}_0$ ($x_0$, $y_0$, $z_0$) with the angle $\phi$, the orientation of point $p$ can be derived as

$$\boldsymbol{p}_\phi = \boldsymbol{R}_\phi \boldsymbol{p}_0, \tag{40}$$

where

$$\boldsymbol{R}_\phi = \begin{bmatrix} \cos\phi+\lambda^2(1-\cos\phi) & \lambda\mu(1-\cos\phi)-\nu\sin\phi & \nu\lambda(1-\cos\phi)+\mu\sin\phi \\ \lambda\mu(1-\cos\phi)+\nu\sin\phi & \cos\phi+\mu^2(1-\cos\phi) & \mu\nu(1-\cos\phi)-\lambda\sin\phi \\ \nu\lambda(1-\cos\phi)-\mu\sin\phi & \mu\nu(1-\cos\phi)+\lambda\sin\theta & \cos\phi+\nu^2(1-\cos\phi) \end{bmatrix}. \tag{41}$$

By substituting $\boldsymbol{p}_0$ into Eq. (35) and Eq. (36), the initial parameters $\theta_{10}$ and $\theta_{20}$ can be obtained. Similarly, by substituting $\boldsymbol{p}_\phi$ into the two equations, $\theta_1$ and $\theta_2$ during the precession polishing process can be determined.

## 6 An example

Due to the unique movement and process parameters of precession polishing, specialized Tool Path Generator software is developed to automatically generate the G-M code for a surface with different process parameters, modes and trajectories. For the hardware platform, a PC-based Open-CNC system with an “IPC+PMAC” structure is adopted. By using this structure, the system software and the data processing ability of the IPC and the real-time control ability of the PMAC can be completely utilized. The software platform can be divided into a management model consisting of a human-machine interactive interface and a trajectory simulation interface, and a control model that provides decoding, coordinate conversion, kinematics conversion, servo control model and auxiliary functions according to the modularized design principle. The structure of the hardware platform is shown in Fig. 17 and a data-flow diagram of the software platform is shown in Fig. 18.

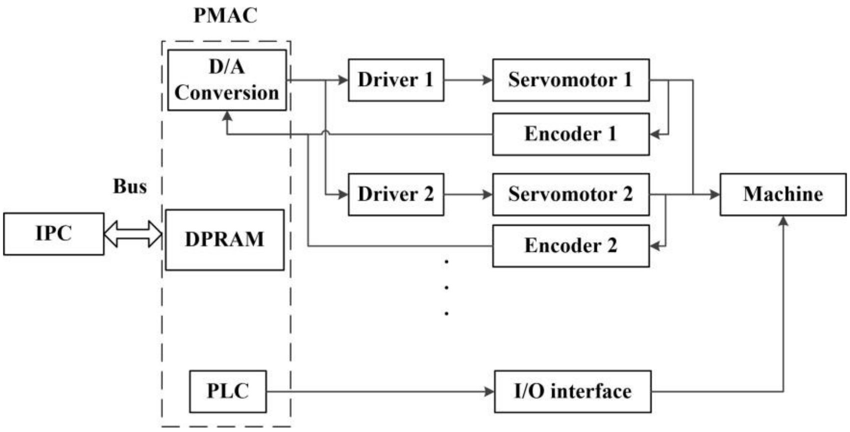

Fig.17 Structure of the hardware platform

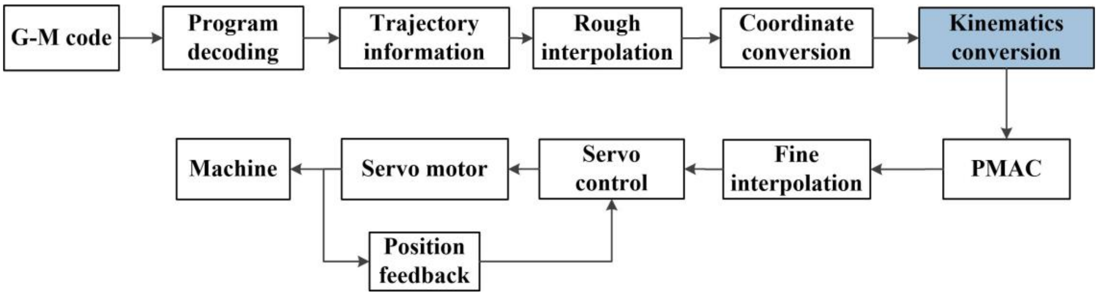

Fig. 18 Data-flow diagram of the software platform

A saddle surface is selected as an example, a simulation is conducted to show the movement of the actuators in the proposed polishing machine based on the established kinematic model. Mathematically, the saddle surface is described by $z\left(x,y\right)=x^2/2p-y^2/2q$ with $p$=200 and $q$=200. The polishing area is 100 mm × 100 mm as shown in Fig. 19. The height between the center of the surface and the workpiece frame $P\text{-}X_wY_wZ_w$ is 20 mm. In the following analysis, the orientation vector of the polishing head and the position coordinates of the moving platform are obtained according to the cutter location data of the surface. By using the inverse kinematics model of the parallel module and serial module derived in this paper, the position command of the actuators in the proposed manipulator with respect to this shape is analyzed theoretically.

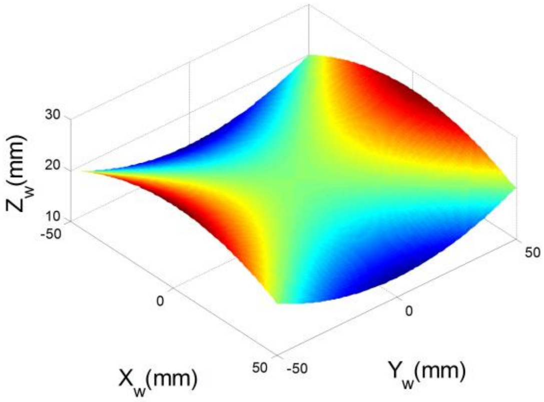

Fig. 19 Saddle surface

A raster polishing path is chosen and the detailed trajectory planning method can be found in the author’s previous study [5]. This surface is polished twice by two mutually perpendicular tracks to obtain randomness. To reduce the number of polishing points during the simulations analysis, the spacing between the points is selected to be 1 mm and the spacing between the traces is selected to be 25 mm. As a result, 761 polishing points are obtained for the selected surface which also involve transition polishing points between the adjacent traces. Without considering the tool size, the polishing points and the normal vector are shown in Fig. 20. The blue lines represent the polishing trajectory and the red dash lines represent the polishing points and the corresponding normal vector. The precession angle is set to $\rho$=15° and inclination angle is set to $\phi$=0°. After post processing, these data can be transferred into the G-M code for the polishing machine.

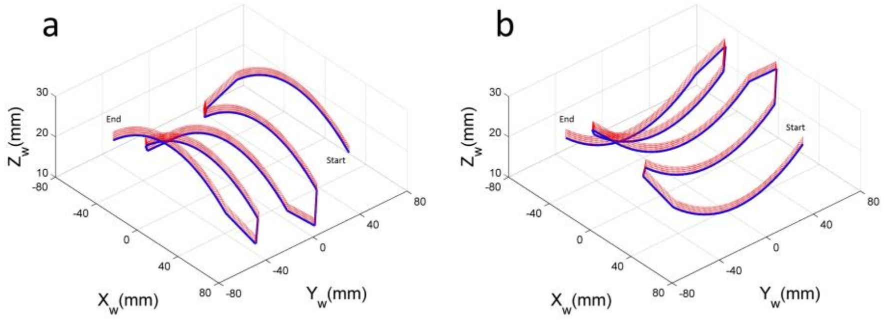

Fig. 20 Polishing trajectory and normal vectors. (a) Trace in $O_w$-$X_wZ_w$ plane. (b) Trace in $O_w$-$Y_wZ_w$ plane.

For the serial module, the angle variation of the actuators is consistent with the motion of the polishing head and the rotation angle can be directly obtained from the angle information in the G-M code, as shown in Fig. 21. For the parallel module, there is a nonlinear relationship between the motion of the workpiece on the platform and the actuators. According to Fig. 9, the initial position of the moving platform is selected on the $O$-$XY$ plane with $Z$ = -600 mm. Assuming the polishing head is connected to the workpieces at this position and the origin of the workpiece frame and the moving platform frame coincide, the motion trajectory of the moving platform can be obtained with $X = X_w$, $Y = Y_w$ and $Z = -Z_w - 600$ from the positon information in the G-M code. By using the inverse kinematic model of the parallel module, the position variation of the actuator of the parallel module is shown in Fig. 22. As it can be seen from Fig. 20(a) and Fig. 22(a), $d_2$ is equal to $d_3$ when the moving platform is in the $O$-$XZ$ plane ($Y$ = 0). This is consistent with the setting of the coordinate system and confirms the validity of the results.

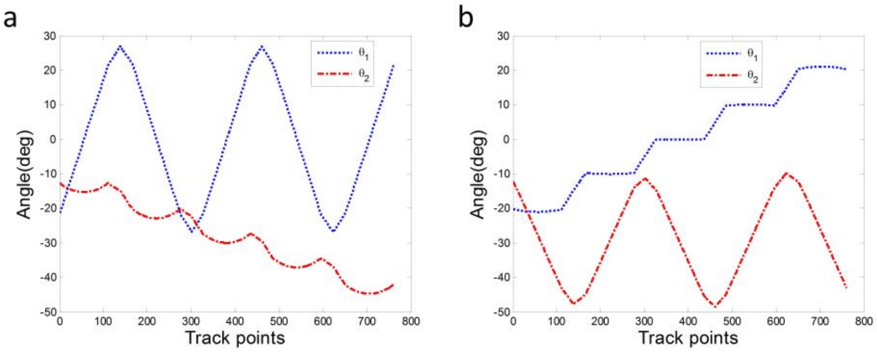

Fig. 21 Angle variation of the actuators on the serial module corresponding to (a) trace in $O_w$-$X_wZ_w$ plane and (b) trace in $O_w$-$Y_wZ_w$ plane.

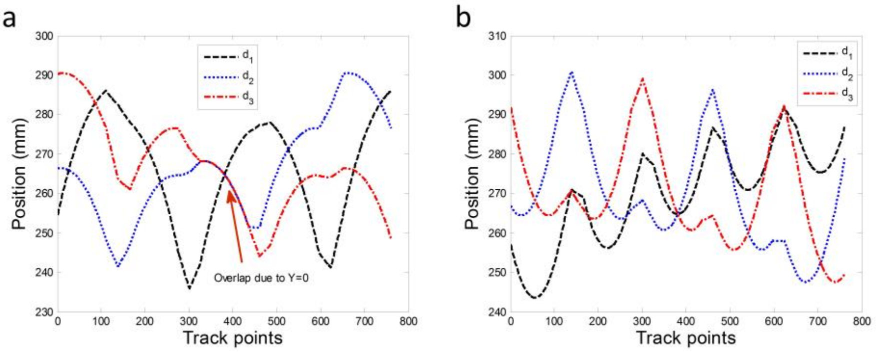

Fig. 22 Position variation of the actuators on the parallel module corresponding to (a) trace in $O_w$-$X_wZ_w$ plane and (b) trace in $O_w$-$Y_wZ_w$ plane.

## 7 Conclusions

Machine tool users usually seek faster, stiffer, more compact and more accurate machines. To overcome the drawbacks of current automated polishing systems, a novel hybrid manipulator for polishing freeform surfaces is proposed. It comprises a two DOF serial module and a three DOF parallel module with a redundant rotation on the moving platform. The advantages of the proposed hybrid manipulator include: (1) the precession polishing process leads to a Gaussian-like tool influence function; (2) decoupled translation and orientation leads to a relatively simple control strategy; and (3) the parallel module leads to greater stiffness and better dynamic performance.

This paper presents a detailed theoretical investigation of machine kinematics. For the parallel module, the solutions for both the inverse and forward kinematics problems are derived and the velocity analysis is performed. A straightforward kinematics model is proposed that has a concise and direct derivation process compared with the equations-based method. Taking into consideration the physical joints' limits, the reachable workspace of the parallel module is generated by using mutually verifying geographical and numerical approaches. The optimal structural parameters to maximize the workspace volume are obtained with $b$ = 100 mm and $\alpha$ = 45°. Dexterity characteristics of the parallel module are investigated in different section planes. The module exhibits mirror symmetry with respect to the $X$-axis and 120° centrosymmetry with respect to the $Z$-axis. In a plane at a given height, the dexterity decreases when the moving platform moves from the center to the boundary. For the serial module, the kinematics model, workspace and precession analysis is conducted according to the topological structure. An example of saddle surface finishing with this manipulator is given. The motion of the actuators with respect to this shape is analyzed theoretically and the validity of the results is confirmed by simulations. This study provides an important means in the design of the polishing machines.

## Acknowledgement

The authors would like to express their sincere thanks to the Innovation and Technology Commission (ITC) of the Government of the Hong Kong Special Administrative Region (HKSAR) for the financial support of the research work under the projects No. GHP/031/13SZ. The work was also supported by the National Science Foundation of China (Grant No. 51305104), Shenzhen Research Funds (Grants No. SGLH20131010144128266 and ZDSYS20140508161825065) and a PhD studentship (project account code: RU98) from The Hong Kong Polytechnic University.

## Reference

[1] Thompson KP, Rolland JP. Freeform optical surfaces: a revolution in imaging optical design. Optics and Photonics News, 2012, 23(6): 30-35.

[2] Márquez JJ, Pérez JM, Rıos J, Vizán A. Process modeling for robotic polishing. Journal of Materials Processing Technology, 2005, 159(1): 69-82.

[3] Cheung CF, Ho LT, Charlton P, Kong LB, To S, Lee WB. Analysis of surface generation in the ultraprecision polishing of freeform surfaces. Proceedings of the Institution of Mechanical Engineers, Part B: Journal of Engineering Manufacture, 2010, 224(1): 59-73.

[4] Cheung CF, Kong LB, Ho LT, To S. Modelling and simulation of structure surface generation using computer controlled ultra-precision polishing. Precision Engineering, 2011, 35(4): 574-590.

[5] Lin WY, Xu P, Li B, Yang XJ. Path planning of mechanical polishing process for freeform surface with a small polishing tool. Robotics and Biomimetics, 2014, 1(1): 1-15.

[6] Pan R, Zhang YJ, Cao C, Sun M, Wang ZZ, Peng YF. Modeling of material removal in dynamic deterministic polishing. The International Journal of Advanced Manufacturing Technology, 2015: 1-12.

[7] West SC, Martin HM, Nagel RH, Young RS, Davison WB, Trebisky TJ, et al. Practical design and performance of the stressed-lap polishing tool. Applied Optics, 1994, 33(34): 8094-8100.

[8] Zhao HS, Fan B, Li XJ, Zeng ZG. Surface accuracy analysis of active stressed lap based on structure function. Optical Review, 2015, 22(1): 52-57.

[9] Zhang JF, Li B, Wang B, Dong S. Analysis on formation mechanism of ultra-smooth surfaces in atmospheric pressure plasma polishing. The International Journal of Advanced Manufacturing Technology, 2013, 65(9): 1239-1245.

[10] Deng H, Monna K, Tabata T, Endo K, Yamamura K. Optimization of the plasma oxidation and abrasive polishing processes in plasma-assisted polishing for highly effective planarization of 4H-SiC. CIRP Annals-Manufacturing Technology, 2014, 63(1): 529-532.

[11] Sidpara A, Jain VK. Theoretical analysis of forces in magnetorheological fluid based finishing process. International Journal of Mechanical Sciences, 2012, 56(1): 50-59.

[12] Li LX, Zheng LG, Deng WJ, Wang X, Wang XK, Zhang BZ, et al. Optimized dwell time algorithm in magnetorheological finishing. The International Journal of Advanced Manufacturing Technology, 2015, 81(5): 833-841.

[13] Walker DD, Beaucamp ATH, Bingham RG, Brooks D, Freeman R, Kim S, et al. Precessions process for efficient production of aspheric optics for large telescopes and their instrumentation. Astronomical Telescopes and Instrumentation, 2003: 73-84.

[14] Walker DD, Brooks D, King A, Freeman R, Morton R, McCavana G, et al. The ‘Precessions’ tooling for polishing and figuring flat, spherical and aspheric surfaces. Optics Express, 2003, 11(8): 958-964.

[15] Li B, Hu Y, Wang H. Analysis and simulation for a parallel drill point grinder. The International Journal of Advanced Manufacturing Technology, 2007, 31(9): 915-925.

[16] Li B, Li GT, Lin WY, Xu P. Design and constant force control of a parallel polishing machine. In: Proceeding of IEEE international conference on information science and technology; 2014, p. 324-328.

[17] Cheng G, Yu JL, Gu W. Kinematic analysis of 3SPS+1PS bionic parallel test platform for hip joint simulator based on unit quaternion. Robotics and Computer-Integrated Manufacturing, 2012, 28(2): 257-264.

[18] Cheng G, Xu P, Yang DH, Liu HG. Stiffness analysis of a 3CPS parallel manipulator for mirror active adjusting platform in segmented telescope. Robotics and Computer-Integrated Manufacturing, 2013, 29(5): 302-311.

[19] Wang MX, Liu HT, Huang T, Chetwynd DG. Compliance analysis of a 3-SPR parallel mechanism with consideration of gravity. Mechanism and Machine Theory, 2015, 84: 99-112.

[20] Xie FG, Liu XJ, You Z, Wang JS. Type synthesis of 2T1R-type parallel kinematic mechanisms and the application in manufacturing. Robotics and Computer-Integrated Manufacturing, 2014, 30(1): 1-10.

[21] Tanev TK. Kinematics of a hybrid (parallel-serial) robot manipulator. Mechanism and Machine Theory, 2000, 35(9): 1183-1196.

[22] Kanaan D, Wenger P, Chablat D. Kinematic analysis of a serial-parallel machine tool: The VERNE machine. Mechanism and Machine Theory, 2009, 44(2): 487-498.

[23] Son S, Kim T, Sarma SE, Slocum A. A hybrid 5-axis CNC milling machine. Precision Engineering, 2009, 33(4): 430-446.

[24] Wang GL, Wang YQ, Zhao J, Chen GL. Process optimization of the serial-parallel hybrid polishing machine tool based on artificial neural network and genetic algorithm. Journal of Intelligent manufacturing, 2012, 23(3): 365-374.

[25] Yang J, Altintas Y. Generalized kinematics of five-axis serial machines with non-singular tool path generation. International Journal of Machine Tools and Manufacture, 2013, 75: 119-132.

[26] Preston F. The theory and design of plate glass polishing machine. Journal of the Society of Glass Technology, 1927, 11, 214-256.

[27] Huang Z, Kong L F, Fang Y F. Theory of parallel robotic mechanisms and control. Beijing: China

Machine Press, 1997.

[28] Stock M, Miller K. Optimal kinematic design of spatial parallel manipulators: application to linear delta robot. Journal of Mechanical Design, 2003, 125(2): 292-301.

[29] Chen JS, Hsu WY. Design and analysis of a tripod machine tool with an integrated Cartesian guiding and metrology mechanism. Precision Engineering, 2004, 28(1): 46-57.

[30] Liu XJ, Wang J, Oh KK, Kim J. A new approach to the design of a Delta robot with a desired workspace. Journal of Intelligent and Robotic Systems, 2004, 39(2): 209-225.

[31] Merlet JP. Jacobian, manipulability, condition number, and accuracy of parallel robots. Journal of Mechanical Design, 2006, 128(1): 199-206.

[32] Gao B, Yao YX, Xie DG, Yuan ZJ. Movement modeling and simulation of precession mechanism for bonnet tool polishing. Chinese Journal of Mechanical Engineering. 2006, 42(2):101-104.